Geophysical Journal International

Geophys. J. Int. (2014) **197,** 1484–1499
doi: 10.1093/gji/ggt512
Advance Access publication 2014 February 18

Potential field and bathymetric investigation of the Monowai volcanic centre, Kermadec Arc: implications for caldera formation and volcanic evolution

M. Paulatto,[1] A. B. Watts[1] and C. Peirce[2]

[1] *Department of Earth Sciences, University of Oxford, South Parks Road, Oxford, OX1 3AN, UK. E-mail: michelep@earth.ox.ac.uk*
[2] *Department of Earth Sciences, Durham University, South Road, Durham, DH1 3LE, UK*

Accepted 2013 December 17. Received 2013 December 4; in original form 2013 October 2

SUMMARY

The Monowai volcanic centre, located on the Tonga-Kermadec Arc, consists of a basaltic–andesitic submarine stratovolcano and adjacent caldera. Recent surveys have shown that it is active, but little is known about its structure and evolution. Here we present a combined analysis of swath bathymetry and potential field data from Monowai, acquired during cruise SO215 on the R/V Sonne, in 2011 April–June. The Monowai caldera is associated with a 20–25 mGal Bouguer gravity anomaly high and a broad positive magnetic anomaly. Short-wavelength magnetic anomalies of up to +1400 and –800 nT are observed along the caldera rim and on the summit of the stratovolcano. Inversion of the Bouguer gravity anomaly data shows that the caldera high is caused by a buried dense body consisting of a main unit extending from 3 to 6 km depth, and a shallower ring structure that underlies the rim of Monowai caldera and extends from the seafloor to the top of the main unit. We estimate the average density contrast to be about +450 kg m^{-3}, corresponding to a density of 2650–2850 kg m^{-3}, suggesting a mafic composition. The ring structure is interpreted as set of ring dykes and the main unit as a solidified or partly solidified magma chamber system (the Monowai pluton). The volume of the main unit is estimated to be 200–300 km^3. The observed magnetic anomalies are consistent with magmatic intrusion within the Bruhnes magnetic polarity. Analysis of the swath bathymetry data shows that Monowai is located inside a 20-km-wide graben, part of an en-echelon, left-stepping horst and graben system that spans the length of the arc and backarc. The Monowai caldera is elongated perpendicular to the direction of rifting, suggesting that it is affected by the regional stress regime. Geomorphological analysis suggests that the caldera consists of a single collapse structure and that its complex shape and multiple ring faults can be attributed to prolonged activity and multiple collapse episodes. It remains unclear whether the current eruption at the Monowai cone is fed directly from a small underlying magma chamber, or laterally from a magma body adjacent to the Monowai pluton. However, observation of radial fissure ridges on its flanks suggests that a shallow magma body may have been recently emplaced beneath the summit causing inflation and the formation of extensional cracks.

Key words: Gravity anomalies and Earth structure; Magnetic anomalies: modelling and interpretation; Geomorphology; Volcanic arc processes; Pluton emplacement; Calderas.

1 INTRODUCTION

Submarine volcanic calderas are important sources of volcanic hazard, yet they are not as well understood as their subaerial counterparts, due to the difficulty in accessing them and collecting data and samples. Recent advances have resulted from a renewed interest in the associated hydrothermal systems, which have been recognized as potential targets for mineral exploration (e.g. de Ronde *et al.* 2005). Attention has been focused on the Tonga–Kermadec arc (e.g. Massoth *et al.* 2007; Graham *et al.* 2008) that comprises 12 volcanic islands and at least 37 submarine volcanic centres. Most of these are known to be volcanically or hydrothermally active and many comprise submarine calderas and are potential sources of volcanic and tsunami hazard. Many were discovered only recently and only a few have been studied in detail, because of their remoteness. Available data are mostly restricted to rock samples and swath bathymetry, and few constraints exist on their subseabed structure and plumbing systems.

Constraints on the volumes and shapes of active or extinct magma reservoirs and conduits are particularly valuable as they are important parameters in modelling the stability of volcanoes and the conditions that lead to initiation and termination of caldera collapse (e.g. Roche & Druitt 2001; Geyer *et al.* 2006). Potential field measurements at volcanic calderas have helped understand the dynamic evolution of shallow magma chamber emplacement and caldera formation (e.g. Rymer & Brown 1986). Magnetic anomalies can be used to identify volcanic conduits and areas affected by hydrothermal alteration. Hydrothermally altered basalt is typically characterized by a reduction in magnetization compared to unaltered basalt, as interaction with hydrothermal fluids gradually replaces titanomagnetite with sulphide minerals (e.g. Tivey & Dyment 2010). Gravity anomalies can be used to determine density variations in the subsurface and delineate volcanic and tectonic structures, particularly where additional constraints from magnetic anomalies, seismic reflection and refraction profiles and other geological data are available.

Calderas on land are associated with both positive (up to +30 mGal) and negative (up to –60 mGal) Bouguer gravity anomalies (Table 1). Bouguer gravity anomaly 'lows' have been variously attributed to subsidence, shallow partial melt bodies and low-density sediments. They are characteristic of silicic calderas, associated with explosive eruptions which deposit large volumes of highly porous ignimbrites. On the other hand, Bouguer gravity anomaly 'highs' have been attributed to the contrast between dense shallow plutons and less dense host rock, which may be less mafic or more porous. They are usually associated with basaltic or basaltic-andesitic calderas and effusive eruption styles (Rymer & Brown 1986). Some calderas cannot be clearly classified in these terms, as often the Bouguer anomaly is a combination of effects such as a short-wavelength negative anomaly arising from caldera collapse and sediment infill, and a longer-wavelength positive anomaly from a dense underlying pluton (e.g. Guayabo caldera, Costa Rica, Hallinan 1991, 1993; Krakatoa, Indonesia, Deplus *et al.* 1995).

Few constraints exist on gravity anomalies and subsurface density variations at submarine calderas. Here we examine gravity and magnetic data from the Monowai volcanic centre, in the Kermadec Arc (Fig. 1). Monowai comprises an active stratovolcanic cone and one of the world's largest submarine calderas. The gravity and magnetic data presented here were collected, together with swath bathymetry data, during cruise SO215 of the R/V Sonne in 2011 April–June. We use these data to place constraints on the shallow structure of the cone and caldera, the mechanisms of their formation and the links that might exist between hydrothermal activity, volcanism, and the pre-existing tectonic fabric of the region.

2 PREVIOUS WORK AT MONOWAI

The Monowai volcanic centre is located approximately mid-way along the Tonga-Kermadec Arc, proximal to the collision zone between the arc and the Louisville Ridge seamount chain (Fig. 1a), 190 km west of the trench and 110 km above the subducting Pacific oceanic Plate (Hayes *et al.* 2012). The volcanic centre is entirely submarine and comprises a 12×9 km caldera complex (Monowai caldera) and a 1500 m high stratovolcano (Monowai cone), plus several parasitic cones covering an area of 400 km^2 (Fig. 1b).

The presence of an active submarine volcano was recorded as early as 1877 (Wright *et al.* 2008) but it was not until 1977–1979 that Monowai was surveyed with modern instrumentation. Following observations of volcanic activity by maritime patrol aircraft in 1977, the HMNZS Monowai carried out a single-beam bathymetry survey and detailed observations of activity at the sea surface. At the time, only Monowai cone was recognized (Davey 1980). Subsequent expeditions in 1986, 1998, 2004 and 2007 revealed the presence of the adjacent Monowai caldera and provided detailed bathymetric constraints and a wealth of other geological and geophysical data (Table 2).

Monowai cone (MoV, Fig. 1b) is the site of current volcanic activity as demonstrated by observations of water discoloration,

Table 1. Summary of positive and negative Bouguer gravity anomalies over calderas.

Caldera	Wavelength (km)	Amplitude (mGal)	Caldera width (km)	References
Calderas with positive Bouguer anomalies				
Masaya Caldera, Nicaragua	20	+30	11×5	Connor & Williams (1990)
Medicine Lake, California	>20	+27	>10	LaFehr (1965), Finn & Williams (1982)
Monowai	20	+20–25	12 × 9	This paper
Kilauea, Hawaii	16–40	+15	4	Ryan *et al.* (1981) Fumerato *et al.* (1976)
O-Sima, Japan	5–15	+15	5	Yokoyama & Tajima (1957) Yokoyama (1969)
Newberry Volcano	40	+12	5–7	Gettings & Griscom (1988)
Poas, Costa Rica	1.6	+8	1	Rymer (1985)
Vulcano, Tyrrhenian Sea	3	+6	2	Budetta *et al.* (1983)
Calderas with negative Bouguer anomalies				
Yellowstone, Wyoming	>80	–60	75	Eaton *et al.* (1975)
Lake Toba, Sumatra	70	–56	70× 20	Nishimura *et al.* (1984)
Kuttyaro, Japan	>16	–46	22	Yokoyama (1958)
Long Valley, California	40	–40	40 ×15	Kane *et al.* (1976)
Aira, Japan	20	–30	22	Yokoyama (1961)
Aso, Japan	15–20	–20	25	Yokoyama (1963)
Mono Basin, California		–20	19	
Tota, Japan	>12	–14	12	
Hakone, Japan		–10	11	
Krakatoa, Sumatra	8	–9	10	Deplus *et al.* (1995)
Santorini	12	–8	5–10	Lagios *et al.* (2013)

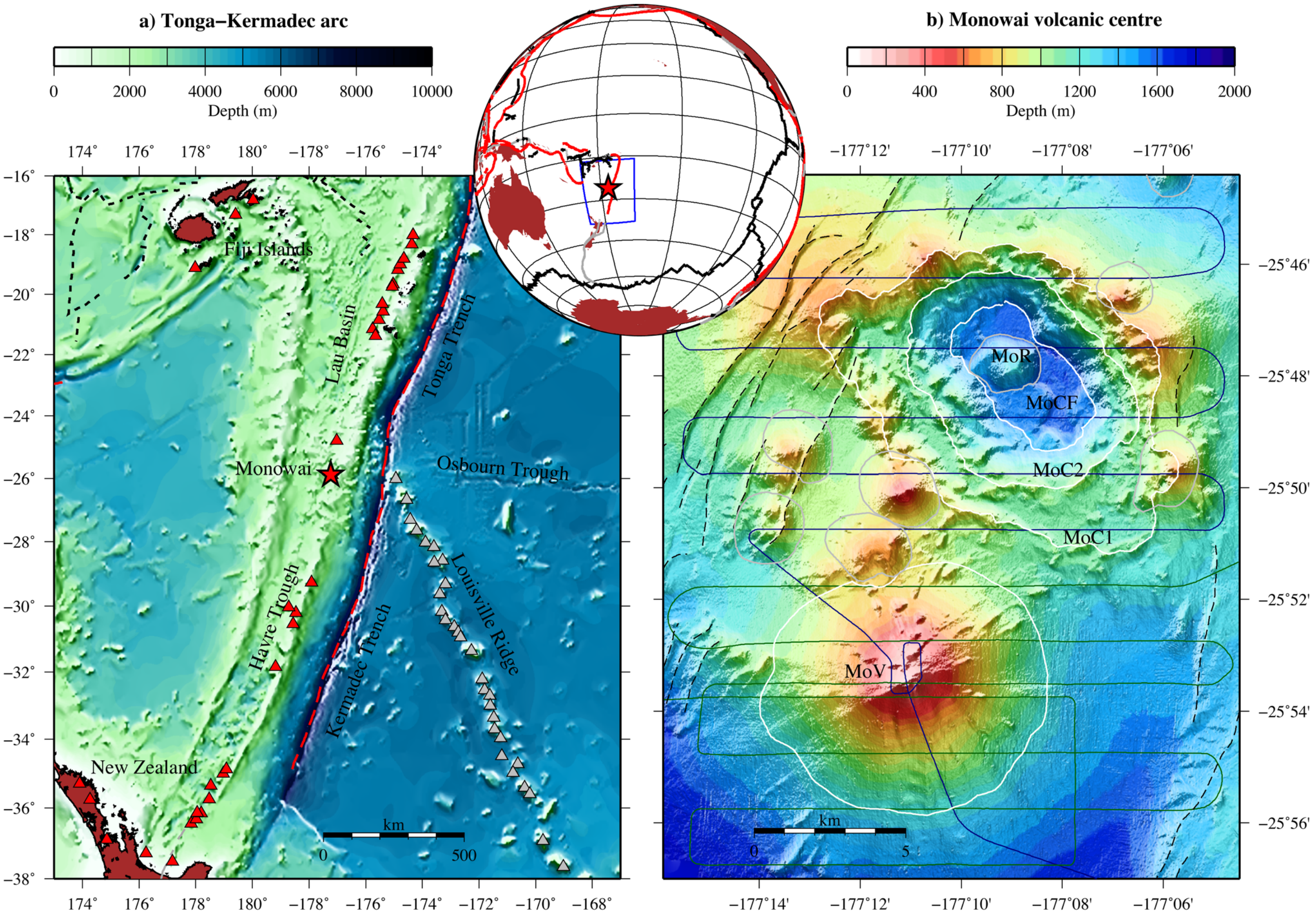

Figure 1. (a) Tectonic setting. Bathymetric map of the Tonga-Kermadec subduction zone showing the main geological features and tectonic boundaries. (b) Monowai volcanic centre showing a compilation of swath bathymetry data sets. MoV, Monowai cone; MoC1, outer Monowai caldera; MoC2, inner Monowai caldera; MoR, central dome; MoCF, caldera floor. The ship tracks of the 2011 survey are marked in blue (Part 1: 2011 May 14) and green (Part 2: 2011 June 1–2). Dashed black lines mark outcropping faults. Inset shows the location of the study area in the SW Pacific.

Table 2. Scientific expeditions at Monowai from 1977 to 2011. References: [1]: Davey (1980); [2]: Wright *et al.* (2008); [3]: Haase *et al.* (2002); [4]: Graham *et al.* (2008); [5]: Embley *et al.* (2005); [6]: Chadwick *et al.* (2008); [7]: Contreras-Reyes *et al.* (2011); [8]: Watts *et al.* (2012) and this study.

Date	Vessel	Cruise ID	Data collected	Ref.
1977–1979	HMNZS Monowai		Single-beam bathymetry	[1]
1978–1979	HMNZS Tui		Towed sonar array	[1]
1986	RV T. Washington		Swath bathymetry	[2]
1998 September	R/V Sonne	SO135	Swath, dredging	[3]
2004 September	R/V Tangaroa	NZAPLUME III	Swath, dredging, ROV	[2,4]
2005	R/V Ka‘imikai-o-Kanaloa	NZASRoF	PISCES submersible	[5]
2007 April 27 to May 17	R/V Sonne	SO192 - MANGO	Swath, ROV, coring	[6]
2008 January 7 to February 16	R/V Sonne	SO195a - TOTAL	Swath	[7]
2011 May 14 to June 2	R/V Sonne	SO215	Swath, gravity, magnetics	[8]

degassing, flank instability, changes in bathymetry and detection of *T* waves (Stoffers *et al.* 1999; Embley *et al.* 2005; Watts *et al.* 2012). Repeat bathymetric surveys have revealed ongoing changes in the topography of the volcano since at least 1998, including several flank collapse scarps and associated debris flow deposits, and the intermittent growth of lava domes or cones at the top of the volcano shifting the summit to the south by several hundred metres between 1978 and 2011 (Chadwick *et al.* 2008; Wright *et al.* 2008; Watts *et al.* 2012). Monowai cone is roughly conical, 12 km in diameter, and rises from a depth of 1700 m depth at its base to 60 m depth at the summit in 2011. The summit is marked by a 1200-m-long, north–south trending ridge resulting from the southward migration of the eruptive vent (Watts *et al.* 2012). The summit in 2011 was located at the southern end of the ridge and consisted of a sharp conical spine with slopes of over 60° in the centre of an arcuate collapse scarp. The creation of the spine, witnessed during SO215 in 2011 May–June, happened over 5 d and was accompanied by intense hydro-acoustic activity, documented by *T*-wave recordings on local and distant IRIS seismic stations and contemporaneously deployed ocean-bottom seismographs (Watts *et al.* 2012).

The summit is highly unstable as witnessed by the frequent flank collapses (Chadwick *et al.* 2008; Wright *et al.* 2008) and observations of continuous wasting of turbidity currents during ROV dives in 2007 May (Flueh & Kopp 2007).

Monowai caldera is a large depression to the NNE of Monowai cone, with its floor at ∼1600 m depth and surrounded by a system of ring faults. The caldera complex has been interpreted as two main nested calderas (Graham *et al.* 2008). The larger one (MoC1, Fig. 1b) has a volume of 27.8 km^3 and extends over an area of 12 × 9 km. The smaller inner caldera (MoC2) has a volume of 8.9 km^3 and extends over an area of 7 × 5 km. The floor, rim and flanks of the caldera complex are covered by numerous parasitic cones ranging in size from 100 m to a few kilometres in diameter. Some most likely predate the caldera formation as they have been dissected by the ring faults; others are intact and may have formed over fissures running around the caldera rim (Graham *et al.* 2008). The top of the outer rim of the caldera wall is at 500–1000 m depth. At the centre of the caldera lies a mound (MoR) with a 2000 m diameter and rising 250 m above the surrounding caldera floor. This mound has been interpreted as a resurgent dome (Graham *et al.* 2008; Timm *et al.* 2011). It is not clear when the caldera last erupted, but ongoing magmatic-hydrothermal activity suggests elevated temperature in the shallow crust (Embley *et al.* 2005; Leybourne *et al.* 2012).

Monowai has been sampled with dredges and submersible dives providing constraints on the petrology of eruptives. Recovered samples range from pillow lavas to scoria that are often highly vesicular. The volcanic products of Monowai cone are entirely tholeitic basalt (bulk-rock silica 49–51 wt per cent), while those from Monowai caldera are more evolved and range from tholeitic basalts to andesites (bulk-rock silica 50–63 wt per cent Graham *et al.* 2008; Timm *et al.* 2011).

3 DATA ACQUISITION

Our 2011 swath bathymetry and potential field survey comprised two parts. Part 1 (May 14) covered Monowai caldera and the summit of Monowai cone, while Part 2 (June 1–2) covered the summit and flanks of Monowai cone (Fig. 1b).

3.1 Bathymetry data

The swath bathymetry data were collected using a Kongsberg-Maritime EM120 multibeam sonar system calibrated using a sound velocity profile measured at 27°47.9′S/175°56.9′W. To assess the resolution of the acquired data, we selected an area of repeat coverage away from the cone and caldera and calculated the mean and rms difference between the two passages over the same area. An rms difference of 6.3 m for the raw data was observed. After hand editing, the rms difference was reduced to 3.4 m, which we believe is representative of the data accuracy. The data were merged with all other available swath bathymetry data for Monowai and the surrounding region (Table 2) and the resulting data set was reprocessed and gridded using MB-System (Caress & Chayes 1995) and the Generic Mapping Tools (GMT, Wessel & Smith 1991) covering an area of 50 × 65 km with grid spacing of 20 × 20 m.

To aid the interpretation of geomorphological features we calculated a range of morphometric functions including slope, aspect, plan curvature and rugosity (e.g. Micallef *et al.* 2007; Wilson *et al.* 2007), using tools from GMT, IVS3D Fledermaus and GRASS (Neteler *et al.* 2011; Fig. 2). Aspect is the direction of the maximum slope and is particularly useful for identifying subtle tectonic lineaments. Plan curvature is the curvature of the seabed surface in the horizontal plane and can be used to identify faults, scarps and ridges. Rugosity is a measure of surface roughness, given by the ratio between surface area and projected area within a cell, and aids the identification of seabed fabric, for example, volcanic fields and sediment-covered areas. Based on these functions we were able to identify and map tectonic and volcanic features on and around the volcanic centre, including volcanic cones, volcanic fissure ridges, faults, cliffs and valleys.

3.2 Gravity data

The gravity data were acquired using a LaCoste & Romberg Air-Sea gravimeter system (Model S-40). The measurement locations were determined to ∼2 m accuracy by the ship's differential GPS system. We used Lacoste's 1 s 'QC-gravity' which was calculated from beam motions electromagnetically damped to eliminate strong horizontal and vertical accelerations induced by the ship's motion. The QC-gravity data were re-sampled to 10 s and processed with navigation and ship motion data to correct for the Eötvos error, calculated from the ship's latitude, heading and speed, and the cross-coupling error, calculated from the horizontal and vertical accelerations acting on the beam. The processed gravity data were corrected for instrument drift and converted to absolute gravity accelerations by performing a tie with gravity base stations in Auckland (New Zealand) and Townsville (Australia). The free-air gravity anomaly was then calculated by subtracting the 1984 International Gravity Formula for a rotating ellipsoid (Fig. 3) with flattening of 1/298.25.

The free-air gravity anomaly was filtered with a 400 s convolution cosine filter to remove short-period noise introduced by yaw-induced scatter in the Eötvos correction. Testing of different filter widths showed that a 400 s filter produces a free-air gravity anomaly that correlates best with both Lacoste's QC-gravity and the topography, and fully removes the short-period noise (Fig. 4). There is a significant difference of up to 15 mGal between the satellite-derived gravity anomaly, which shows a free-air gravity anomaly high of +10 mGal over the Monowai caldera, and the shipboard-derived free-air gravity anomaly, which shows a −12 mGal low (Figs 5a and b). This difference is attributable to the much better resolution of shipboard gravity anomaly data at short wavelengths.

The accuracy was assessed by calculating the difference between repeat measurements at intersecting ship tracks (cross-over points). Over the whole cruise ∼2700 cross-over points occurred with a mean difference of −1.0 mGal and an rms difference of 7.2 mGal. Around Monowai 13 cross-over points were identified with a mean cross-over error of 1.2 mGal and an rms of 7.9 mGal. The noise level is higher for part 2 of the survey, carried out in June, due to heavier seas and a stronger swell.

The free-air gravity anomaly data were gridded over an area of 23 × 19 km over the Monowai volcanic centre using b-spline polynomials and a regular grid spacing of 200 × 200 m. Unsurprisingly, the resulting anomaly shows a strong correlation with topography. There is a broad high over the volcanic centre, with localized gravity anomaly highs of +134 mGal over the cone summit and +126 mGal over the caldera rims (Fig. 5a). The caldera depression is associated with a relative gravity low.

3.3 Magnetic data

Total magnetic field data were collected with a SeaSPY proton precession magnetometer towed 220 m astern of the ship at a depth of

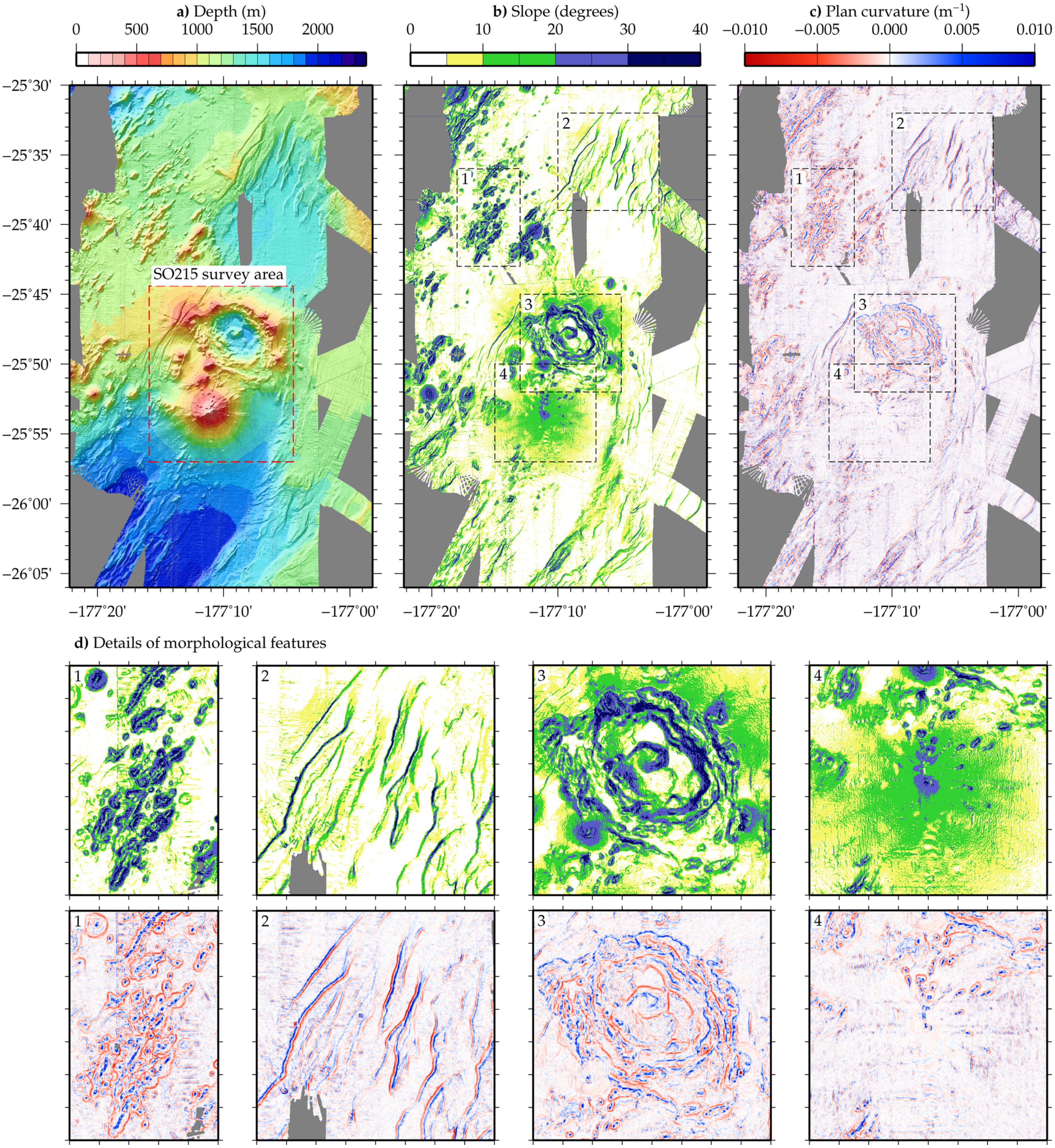

Figure 2. Geomorphic analysis of the Monowai volcanic centre and surrounding seafloor. (a) Bathymetry, the dashed red box marks the area shown in subsequent figures; (b) slope gradient; (c) plan curvature; (d) details of morphological features: (1) volcanic fissure ridges, (2) extensional faults, (3) Monowai caldera complex and (4) Monowai cone.

∼16 m. The magnetic anomaly was calculated by subtracting the regional field predicted using the 2010 International Geomagnetic Reference Field model of the Earth's magnetic field from the observed magnetic field (regional inclination of −49° and declination of 12°). A 20 s median filter was applied to the time-series to remove high-frequency noise. Cross-over error analysis was conducted to estimate the data uncertainty. Unfortunately only a small number of ship track cross-overs occurred in the survey area and these mostly fall near the Monowai cone summit, close to abrupt changes in heading and speed of the ship. Moreover this area was subject to significant addition of volcanic rock very close to the sea surface in the interval between the two parts of the survey (Watts *et al.* 2012). For these reasons cross-over errors in this region are up to 900 nT. Away from the summit, cross-over errors are of the order of 10 nT, which are believed to be more representative of the entire survey uncertainty.

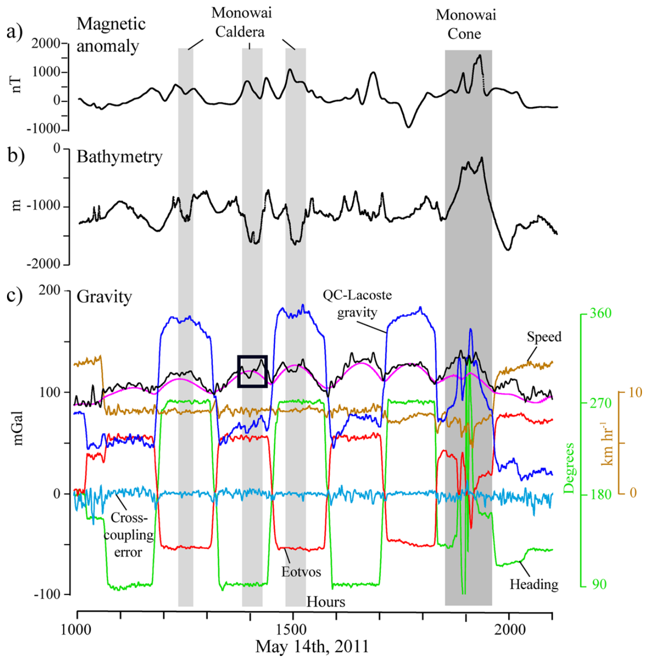

Figure 3. Gravity, magnetic and bathymetry data acquired during 10:00–21:00 GMT on 2011 May 14. See Fig. 1 for profile location. Light grey shade shows where the ship track crossed Monowai caldera. Dark grey shade shows crossings of Monowai cone. (a) Magnetic anomaly. (b) Centre-beam bathymetry. (c) Shipboard and satellite-derived gravity data. The dark blue curve shows the Lacoste-Romberg QC-gravity sampled at 10 s and uncorrected for Eötvos effects. The green curve shows ship heading. The brown curve shows ship speed. The light blue curve shows the cross-coupling error. The red curve shows the Eötvos correction. The black curve shows the free-air gravity anomaly. The purple curve shows the Sandwell & Smith (2009) satellite–derived gravity field (V18.1). The black box marks the data section shown in Fig. 4.

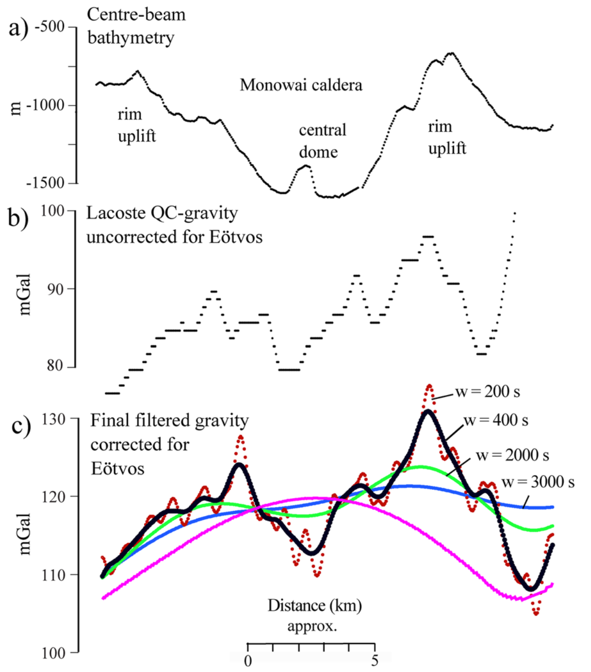

Figure 4. Bathymetry and shipboard and satellite-derived free-air gravity anomaly profile of the Monowai caldera. See Fig. 1 for profile location. (a) Centre-beam bathymetry. (b) Lacoste-Romberg QC-gravity, uncorrected for Eötvos. (c) Final filtered gravity anomaly, corrected for Eötvos and cross-coupling error. The red, black, green and blue curves show the final gravity anomaly with different filter widths. The purple curve shows satellite-derived gravity. A gravity anomaly based on a filter width of 400 s (thick black curve) accounted well for the main features in the Lacoste-Romberg QC-gravity anomaly and showed the best correlation with the short-wavelength topography.

The magnetic anomaly varies between –800 and +1400 nT over the survey area (Fig. 5c). The data were reduced to the pole using a fast Fourier transform (FFT) technique. Reduction to the pole assumes that the observed magnetic anomaly is entirely caused by induced magnetization and transforms it as if the inducing magnetic field had an inclination of 90°. Reduction to the pole has the effect of aligning magnetc anomalies with their sources, allowing to more easily correlate them with geological features on the seafloor (Fig. 5d). Monowai cone is characterized by a magnetic anomaly high with three distinct lobes. The strongest lobe is centred directly above the 2011 summit (MA1+ in Fig. 5c) and reaches +1432 nT. The other two anomalies are centred one 2 km to the west (MA3+) and one 3 km to the northeast (MA2+). Monowai caldera is

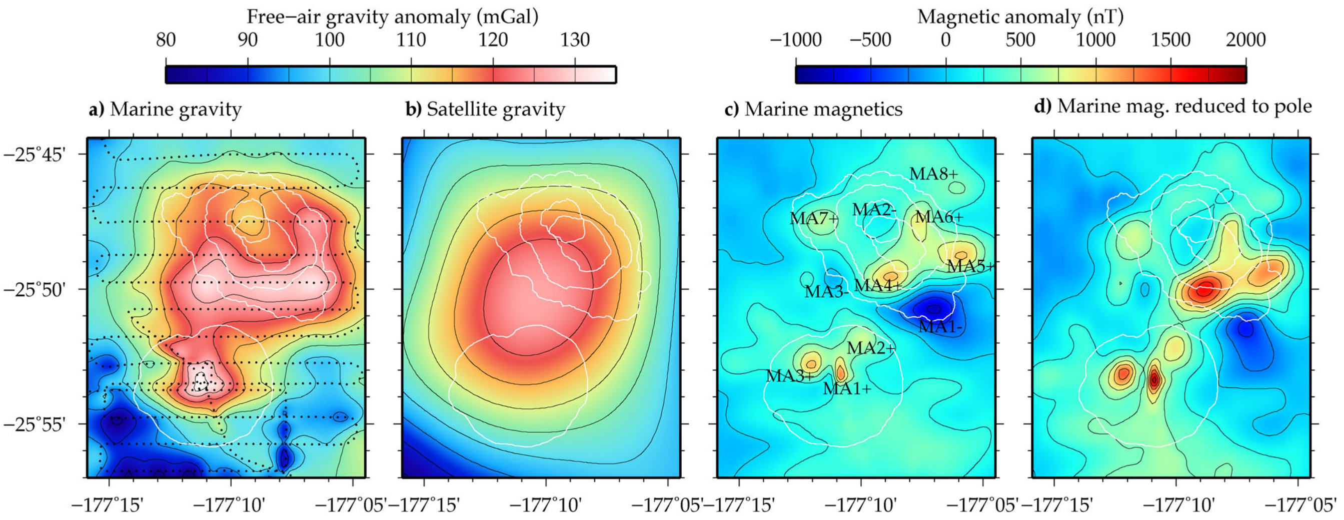

Figure 5. Potential field data at Monowai volcanic centre: (a) free-air gravity anomaly from the 2011 survey; (b) satellite-derived gravity anomaly (Sandwell & Smith 2009); (c) magnetic anomaly from 2011 survey; (d) magnetic anomaly after reduction to the pole. The white lines mark the location of the Monowai cone and Monowai caldera.

characterized by several positive magnetic anomaly highs along the caldera rim (MA4+ to MA7+) and a number of magnetic anomaly lows (MA1− to MA3−). The strongest anomalies in the caldera are located over the southern sector of the rim.

4 ANALYSIS OF THE POTENTIAL FIELD DATA

4.1 Bouguer anomaly

An FFT technique (Parker 1973) was used to remove the gravity effect of the water–rock interface and calculate the Bouguer gravity anomaly assuming a water density of 1030 kg m^{-3} and rock densities in the range 2000–2800 kg m^{-3}. The rock density that best minimizes the correlation between the Bouguer gravity anomaly and topography is 2170 kg m^{-3}. At Monowai cone a rock density of 2170 kg m^{-3} leaves a small positive anomaly at the summit. To completely correct for the gravity effect of the cone topography, the rock density needs to be increased to ∼2400 kg m^{-3}. Unfortunately, there are no density measurements available for rock samples from the Monowai volcanic centre, but typical surface rock types (Timm *et al.* 2011) appear similar to those found at Rumble II Volcano on the Kermadec arc which have an average dry density of 2020 kg m^{-3} and an average porosity of 25.9 per cent (Wright & Gamble 1999). These values lead to a wet density of 2290 kg m^{-3}, which is consistent with the above estimates.

Irrespective of the choice of rock density a number of clear features can be observed in the Bouguer gravity anomaly map (Fig. 6): (i) little or no Bouguer anomaly is present at Monowai cone; (ii) a large Bouguer anomaly high is present over the Monowai caldera with maximum of 20–25 mGal above the regional average and (iii) Bouguer anomaly lows are present to the south of Monowai cone and over the highly faulted region northwest of the caldera. In the following analysis we initially consider a rock density of 2300 kg m^{-3}.

4.2 Gravity inversion method

To quantitatively interpret the gravity anomalies, we carried out an inversion of the Bouguer gravity anomaly data using the least-squares inversion method developed by Camacho *et al.* (2000, 2002, 2011). The approach divides the model domain into a set of prisms and determines the density contrast for each prism with respect to a simple vertical background density profile, which can be constant or a function of depth. The gravity anomaly at each measurement point is described as the combined effect of the vertical gravitational attraction of the prisms, which can be calculated analytically (Pick *et al.* 1973). The size of prisms increases with depth and with distance from the centre of the model. The average prism size is chosen based on the average distance between data points.

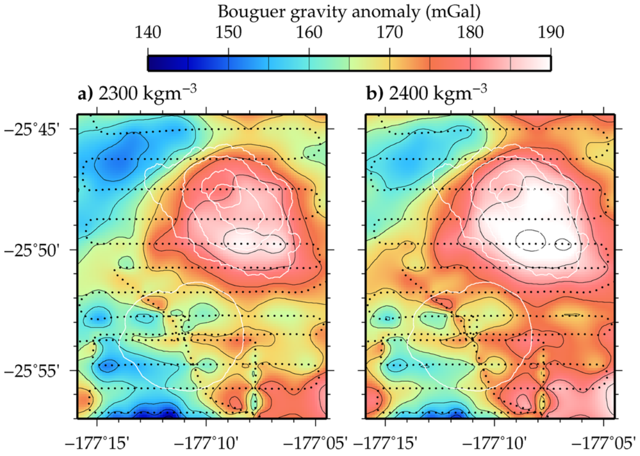

Figure 6. Bouguer anomaly over the Monowai volcanic centre calculated with two different values of rock density: (a) 2300 kg m^{-3}; (b) 2400 kg m^{-3}. The white lines mark the location of Monowai cone and Monowai caldera.

Camacho *et al.* (2011) choose an objective function that combines a least-squares (L2-minimization of the residuals) and a smoothness factor, which effectively corresponds to a minimum-anomalous-mass constraint. The amount of smoothing is controlled by the damping factor λ. In addition, the prism densities are not inverted simultaneously, but in a step-by-step fashion, by aggregation of prisms into growing bodies. Initially, all prisms have null density contrast. Then, at each inversion step k the algorithm tests all prisms individually with a positive or negative density contrast $\Delta\rho = \pm\Delta\rho_0$ and selects the single prism which reduces the objective function by the largest amount through a density scaling factor $f_k > 1$. At each subsequent step a new prism is filled and the scaling factor f_k is reduced until it reaches a value of 1.

The procedure described is equivalent to first introducing a small number of prisms with large density contrast and then gradually increasing the number of prisms while reducing the magnitude of the density contrast until the contribution of any additional prism becomes insignificant. The smoothness constraint in the objective function ensures that a scattered distribution of prisms is penalized and instead lumping of prisms into a number of discrete bodies is favoured.

The inversion algorithm optionally allows to gradually decrease the magnitude of the density anomaly throughout the inversion process via the homogeneity parameter α. At the kth step in the inversion the density contrast is governed by the following equation:

$$\Delta\rho_k = \pm\Delta\rho_0[1 - \mathrm{e}^{(1-f_k)/\alpha}]. \tag{1}$$

For $\alpha \to 0$ the exponent tends to $-\infty$ and the second term tends to zero so that the density anomaly remains constant throughout the inversion. If α is increased the second term is very small early on in the inversion, when f_k is large, but increases as $f_k \to 1$, reducing the value of the density anomaly for new prisms. A large α has the effect of producing smoother and more realistic anomalous density bodies as the prisms that are added later in the inversion are generally on the periphery of anomalous bodies.

4.3 Inversion of the Bouguer gravity anomaly data

The Bouguer gravity anomaly data for Monowai volcanic centre were decimated to a 500 m spacing to reduce the number of data points and produce a more homogeneous measurement distribution. The measurement locations were then converted to a local Cartesian reference frame and the Bouguer correction applied. The mean and a linear regional trend were subtracted from the data to remove the effect of long-wavelength variations in crustal structure. Uncertainties of 1 and 2 mGal were assigned to the data from the first and second parts of the survey, respectively, to reduce the relative contribution of the second part of the survey that suffered from higher noise levels. The subsurface was divided into 4548 prisms with an average side of 838 m (minimum 420 m close to the surface, maximum 1414 m at depth).

A number of factors affect the inversion process and their values need to be carefully considered. We carried out a series of tests to evaluate the effect of the damping factor λ, the magnitude of the density anomaly $\Delta\rho_0$, the rock density ρ_t used for calculating the

Bouguer correction, and the presence or absence of a background density increase with depth. The magnitude of the density anomaly, $\Delta\rho_0$, needs to be fixed *a priori*. If the values are too high the inversion will result in a scheletrical density distribution, with sharp density anomalies separated by large gaps. On the other hand, if the values are too small, the inversion will produce inflated bodies and all prisms will be filled with either a positive or a negative density anomaly masking the real structure.

The damping factor λ controls the amount of smoothing in the model. A low value of λ results in a smoother model and larger residuals, while a large value of λ results in a more detailed model with the risk of fitting small-scale noise. Camacho *et al.* (2011) use a criterion for selecting the damping factor based on the spatial correlation of residuals. This approach assumes that noise is spatially uncorrelated and that any correlated component constitutes the signal. The optimal value of λ is chosen so that it minimizes the autocorrelation at a lag equal to the average measurement spacing. Fig. 7a shows a plot of autocorrelation against damping parameter λ. For most realistic values of density contrast the minimum in autocorrelation is found when $\lambda \simeq 20$–40. However the minimum is unstable due to non-random noise in the southern half of the survey. Therefore, the optimal value of λ was instead selected based on the shape of the L-curve, that is, the curve representing the trade-off between residuals and smoothness.

Fig. 7b shows the L-curve for different values of the density anomaly. For large values of the damping factor (λ) the normalized χ^2 varies widely depending on the choice of density anomaly (bottom right of Fig. 7b), with lower density anomalies achieving a higher degree of fit, because it is inherently difficult to generate a smooth model with high density anomalies. For lower values of λ the normalized χ^2 value decreases faster for models with strong density anomalies and reaches a stable value between 1.5 and 2, showing that the assigned uncertainties have been slightly underestimated. The L-curves do not have a particularly pronounced kink and the value of λ corresponding to the maximum curvature depends on the choice of density anomaly. Nevertheless, if the instability in the top of the curves (top left corner of Fig. 7b) is ignored, a maximum in the curvature can be found for λ between 30 and 40. We prefer a value of $\lambda = 40$, which leads to slightly oversmoothed models, because inversions with $\lambda = 30$ tend to fit some of the correlated noise in the southern half of the survey. For $\lambda = 30$–40 the models with density anomalies of $\sim$450 kg m^{-3} have the best fit (lowest χ^2), but density anomalies ranging from 350 to 500 kg m^{-3} cannot be ruled out based on the χ^2. Therefore, interpretation will be restricted to features that are common to this range of models.

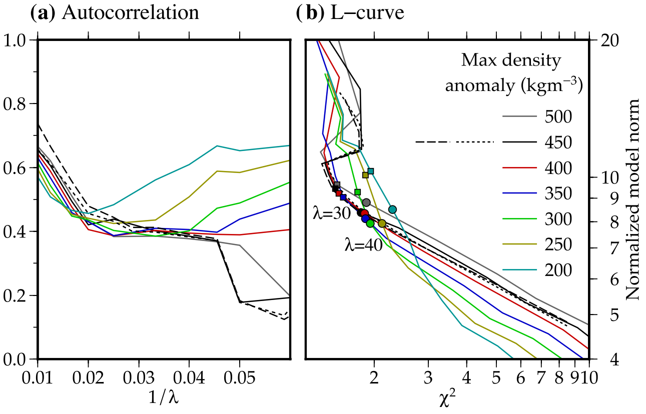

Figure 7. Selection of optimal damping factor. (a) Autocorrelation of the residuals for inversions with varying values of maximum density anomaly are plotted as solid coloured lines while those for inversions with different values of background rock density are plotted with different line pattern. Continuous line: 2300 kg m^{-3}; dashed line: 2400 kg m^{-3}; dotted line: 2170 kg m^{-3}. (b) L-curves for the same models. The squares and circles mark the cases of $\lambda = 30$ and $\lambda = 40$, respectively and are colour-coded following the same palette as the L-curves.

Fig. 8 shows the effect of varying the smoothing parameter λ and the homogeneity parameter α on the inversion results. For $\lambda = 80$ (model a, Fig. 8a), the residuals are significant, with an rms of 3.1 mGal, and are correlated with the Bouguer anomaly, showing that the inversion is unable to reproduce the full complexity of the anomaly pattern. For $\lambda = 40$ (model b, Fig. 8b), the residuals have an rms of 2.2 mGal and are significantly reduced in the northern half of the study area, covered by part 1 of the survey, but they remain higher in the south where the noise level is higher, and close to the model edges where the sensitivity is low. Increasing the homogeneity parameter α from 0 to 6 while keeping λ constant, produces anomalous bodies with more gradual edges (model c, Fig. 8c), but does not affect the general characteristics of the model nor the level of fit or the distribution of residuals (Table 3).

The inversion was repeated for three different values of the rock density suggested by analysis of the Bouguer gravity anomaly: 2170, 2300 and 2400 kg m^{-3}. Changing the terrain density used in the calculation of the Bouguer anomaly within this range has a limited effect on the inversion results (Fig. 7b), showing that although the choice of terrain density is important to estimate the range of absolute densities, it has little influence on the distribution of anomalous mass. The final density models obtained with the different terrain densities are generally very similar, but vary in some of the details.

In the inversions described thus far, the dense body host-rock was assumed to be homogeneous, with a constant density given by the rock density used for the calculation of the Bouguer gravity anomaly. Tonga-Kermadec arc crust appears, however, to be characterized by a strong vertical density gradient in the top 3–4 km below the seabed, associated with unconsolidated sediments with densities of <2000 kg m^{-3} to the igneous basement with density of $\sim$2800 kg m^{-3} (Contreras-Reyes *et al.* 2011). The effect of assuming a homogeneous host rock is that in the deep part of the model the extent of the anomalously dense body is underestimated and its magnitude is overestimated. This results in anomalous bodies that narrow downwards, as in model c (Fig. 9a). The inversion algorithm used in this study allows the simulation of a background vertical density profile defined by a linear or exponential function. We tested a model with a terrain density of 2170 kg m^{-3} and a linear vertical density increase with a gradient of 90 kg m^{-3} km^{-1}, bringing the background density to 2300 kg m^{-3} at the seabed ($\sim$1.5 km depth) and to 2800 kg m^{-3} at 7 km depth (model d, Fig. 9b).

5 GRAVITY INVERSION RESULTS

Although the density models obtained by varying rock density and inversion parameters differ in some of the detailed structure, there are a number of consistent and robust features that can be identified across all of them. The main feature is the relatively high density region beneath Monowai caldera (Figs 9 and 10). It extends over an area of $\sim 9 \times 9$ km and from the seabed to 5 km depth. It is composed of two connected units: a shallow ring structure and an underlying massive body. The ring structure roughly follows the inner caldera rim and has an 8 km diameter. It is wider in the southeast and has a prominent off-shoot to the southwest. The massive body covers a smaller area and is slightly offset to the southeast. It has a rounded

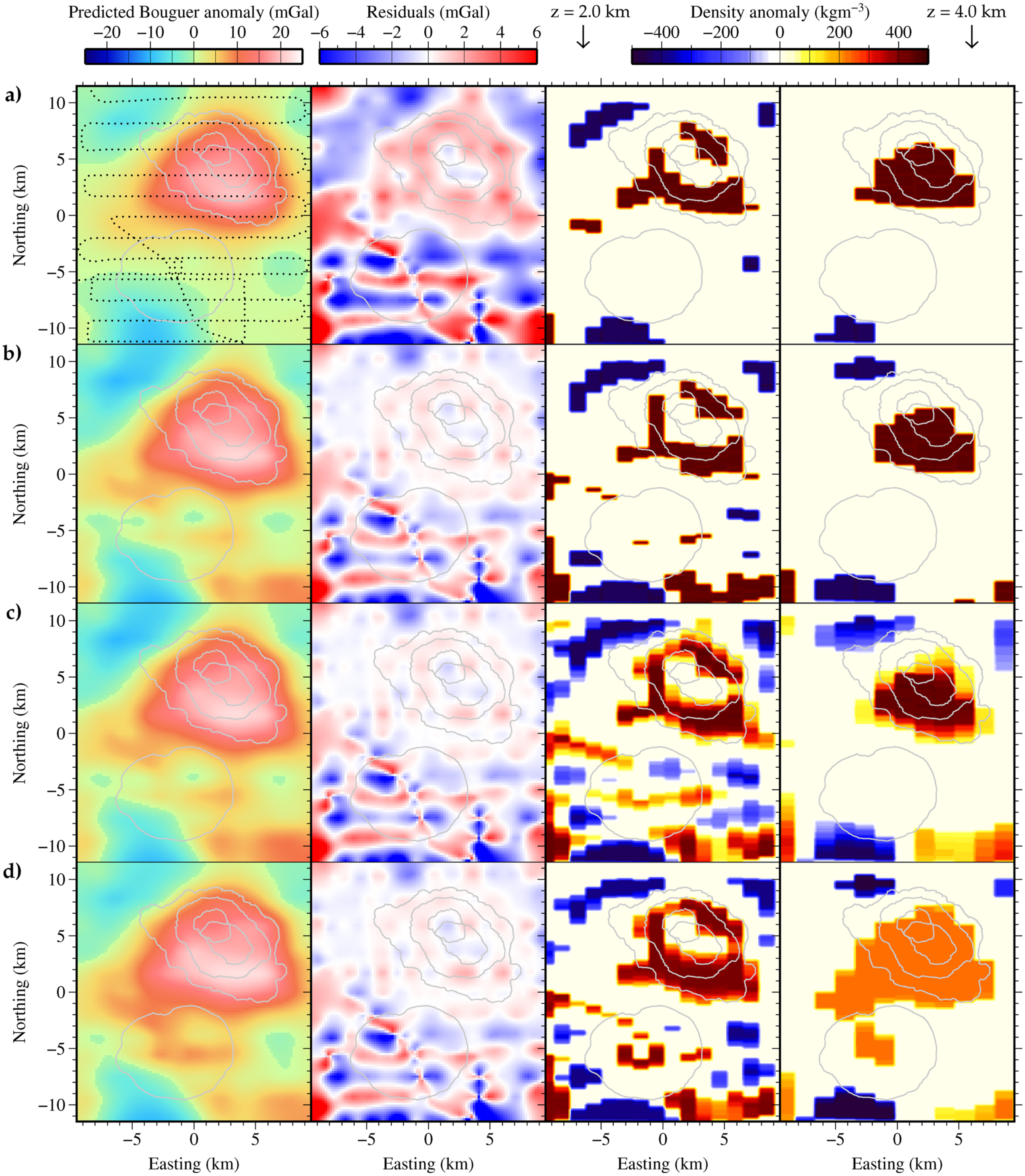

Figure 8. Comparison of inversion results for different values of inversion parameters. The details of each model are listed in Table 3. From left to right: predicted Bouguer gravity anomaly, gravity anomaly residuals, density contrast at 2 km depth, and density contrast at 4 km depth. The main geological features are outlined in grey. The selected measurement locations are marked with black circles along track lines.

base with a diameter of 7 km. Both bodies are characterized by a positive density contrast of about +450 kg m^{-3} which corresponds to an absolute density of ∼2750 kg m^{-3}. The total volume of the high-density body is estimated between 180 and 310 km^3, depending on the choice of inversion parameters and the density threshold used in defining the boundaries of the body. The volume is divided between the deep massive body measuring 120–220 km^3 and the ring structure measuring 60–90 km^3.

A smaller and much weaker anomalous body with a positive density contrast is observed beneath Monowai cone in models with a

Table 3. Model parameters and inversion results for the models shown in Fig. 8.

	a	b	c	d
ρ_t (kg m^{-3})	2400	2400	2400	2170
$\frac{\partial\rho}{\partial z}$ (kg m^{-3}km^{-1})	0	0	0	–90
$\Delta\rho_0$ (kg m^{-3})	450	450	450	400
λ	80	40	40	40
α	0	0	6	4
χ^2	4.40	1.83	1.89	1.74
rms residual (mGal)	3.1	2.2	2.1	2.2

relatively low rock density of 2170 kg m^{-3}. This feature is present but subdued in models with a rock density of 2300 kg m^{-3}, and almost completely absent in models with a rock density of 2400 kg m^{-3}. This body is roughly 2 × 2 km wide and extends from the seabed to ~3.5 km depth and suggests that Monowai cone may have a dense core. A number of regions with negative density contrast are observed to the north and south of the volcanic centre, underlying Bouguer gravity anomaly lows (Fig. 6) and likely corresponding to regions with a thicker volcanoclastic cover.

All of the main features described are still present in the case of a linear background density profile, including a well-defined ring structure overlying the main anomalous body (Fig. 9b). The volume of the shallow ring structure is unaffected, while the volume estimate for the deep main body increases significantly to 200–300 km^3, about 40 per cent larger than for the models with homogeneous background density. The main body is wider and has a flat base and a density contrast which decreases with depth. Since in this case the density contrast for the deeper part of the main body is smaller, the total anomalous mass remains the same.

6 FORWARD MODELLING OF THE MAGNETIC DATA

A simple test to evaluate the validity of our density models is to compute their magnetic effect and compare it to the observed magnetic field. The method of Bhattacharyya (1964) was applied for the calculation of magnetic anomalies due to prism-shaped bodies. A suitable choice of prisms can be used to model both the magnetic effect of the high-density body and the effect of the topography.

First, we calculated the effect of the topography by modelling a uniformly magnetized layer with a horizontal base at 7 km depth and top given by the seabed interface. The magnetic effect of this layer was calculated assuming a 250 × 250 m grid and a total magnetization $m_t = 5.4$ Am^{-1}, corresponding to an apparent magnetic susceptibility of $\chi_t = 0.15$ S.I., assuming no remanent magnetization. This susceptibility was required to match the amplitude of the observed magnetic anomalies. However, the spatial pattern of the observed anomalies could not be reproduced (Fig. 11). Therefore a second model that combined a varying thickness layer and a distribution of magnetized prisms from our density model was tested. As in the previous case we modelled the effect of a varying thickness layer with constant magnetization m_t. Then from density model d (Fig. 8) all prisms with positive density contrast ≥100 kg m^{-3} were selected and assigned an additional constant magnetization m_d. The strength of m_t and m_d were varied to match the observed anomaly (Fig. 11).

Our combined model of a uniformly magnetized topographic layer and a magnetic dense body does match the long-wavelength component of the observed total magnetic field, but does not account for some short-wavelength features (Fig. 11). The best-fitting values of m_t and m_d are 3.2 and 3.6 Am^{-1} respectively, corresponding to apparent magnetic susceptibilities of 0.09 and 0.1 S.I. units, which are at the very high end of typical values for basaltic volcanic rocks (Carmichael 1982). Measured magnetic susceptibilities for fresh dacite samples from Brothers Volcano range from 8.2×10^{-3} to 1.5×10^{-2} S.I. units (Tontini *et al.* 2012), which correspond to an induced magnetization of 0.30–0.55 Am^{-1}. Total magnetization at Brothers Volcano is estimated to be as high as 10 Am^{-1}, corresponding to a Koenigsberger ratio of 20 and showing that remanent magnetization is likely dominating the magnetic anomaly. Remanent magnetization is likely to be similarly important at Monowai, but cannot be reliably estimated in the absence of direct measurements on rock samples.

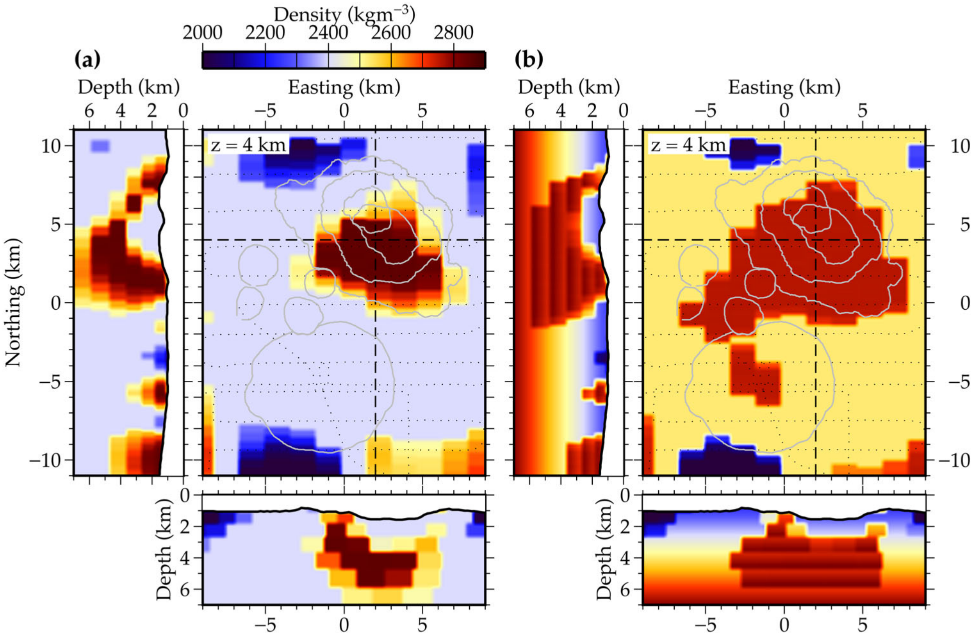

Figure 9. Estimated absolute density of representative density models: (a) cross-sections of model c of Fig. 8 and (b) cross-sections of model d of Fig. 8.

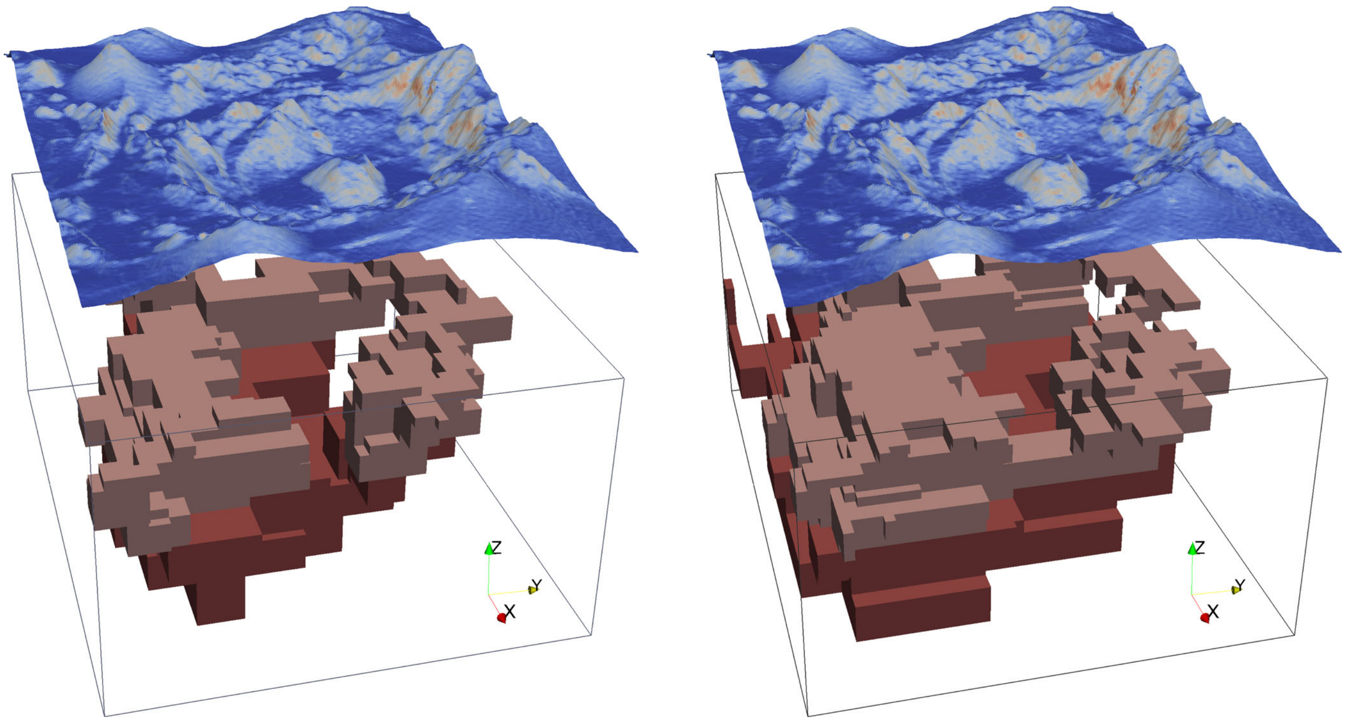

Figure 10. 3-D perspective view of the high-density body beneath Monowai caldera viewed from the east for the two models shown in Fig. 9: (a) model c and (b) model d. The ring structure and the deep massive body are coloured in light brown and dark brown respectively. The topography of the caldera is plotted above and shifted upwards by 2 km to avoid obscuring the high-density body.

The model successfully predicts the long-wavelength magnetic anomaly over Monowai caldera. This has two important implications. First it suggests that the positive density contrast corresponds to intrusive volcanic rocks and has a relatively high apparent magnetic susceptibility, supporting our interpretation that it corresponds to a large mafic intrusion. Second, we can conclude that, to a first-order, the observed anomalies are compatible with a magnetization parallel to the present geomagnetic field, that is, they are consistent with a Brunhes magnetic polarity. Since it is likely that there is a significant component of remanent magnetization this places a maximum age of 0.78 Myr on the buried pluton. Assuming the magmatic instrusion grew over this time period and has a total volume of 200–300 km^3, we can estimate the magmatic flux as 2.5–3.8 × 10^{-4} $\mathrm{km}^3\,\mathrm{yr}^{-1}$.

In general, our combined model overestimates the strength of the magnetic anomalies in the northern and western areas of the caldera and underestimates them in the southern part of the caldera and over Monowai cone. This suggests that there is an increase in magnetization towards the south which is consistent with a younging of the volcanic system in this direction. The older parts of the system would have subdued magnetic anomalies because of the damping effect of a thicker sediment cover and/or relatively low magnetization resulting from hydrothermal demagnetization (Rona 1978). The same mechanism may explain the relative demagnetization observed over the western portion of the caldera rim (MA3−). This region hosts an active low-temperature hydrothermal system and a significant biomass (Leybourne *et al.* 2012).

Over Monowai cone the model is unable to simulate the triple magnetic high and instead results in a broader and weaker anomaly. The sharp magnetic anomalies over Monowai cone are likely due to shallow narrow dykes or cylindrical conduits acting as feeders for summit and flank eruptions. These intrusive structures might have a small density contrast with respect to the surrounding material, most likely consisting of basaltic-to-intermediate volcanic scoria, and are too small to be imaged by the gravity inversion. In contrast, their magnetization is likely to be higher for two reasons. First, since they are intrusive, they may be less strongly affected by demagnetization caused by alteration due to contact with sea water. Second, since they are likely to be young and cooled *in situ*, any remanent magnetization would be aligned with the present geomagnetic field reinforcing the anomaly. A higher resolution magnetic survey would be necessary to constrain the details of the feeder system beneath the cone's summit.

7 DISCUSSION

Irrespective of the large number of parameters in our inverse models, our analysis shows that the positive Bouguer gravity anomaly over Monowai caldera can be explained by a large buried high-density body extending from the seafloor to ∼6 km depth, with a density contrast with the surroundings of ∼450 kg m^{-3}. The absolute density of this body is difficult to constrain from gravity inversion alone, but is likely to be between 2650 and 2850 kg m^{-3}. This range suggests a basic composition such as gabbro (Carlson & Raskin 1984; Christensen & Mooney 1995), as observed, for example, in the layered plutonic complexes of Rum, Skye and Mull, Scotland (Bott & Tuson 1973; Emeleus *et al.* 1996; Troll *et al.* 2000). The vertical extent of the body is also unconstrained. Gravity modelling on Rum suggests steep-sided bodies of dense rock such as gabbro and peridotite extending down to depths of 15 km or more in the crust.

We interpret the deep body as a crystallized or partly crystallized magma chamber system including mafic plutonic rocks and perhaps an ultramafic cumulate base. This large body of magma intruded into low-density host rocks. The composition of the host rocks is unknown, but seismic reflection profile data over the central Tonga

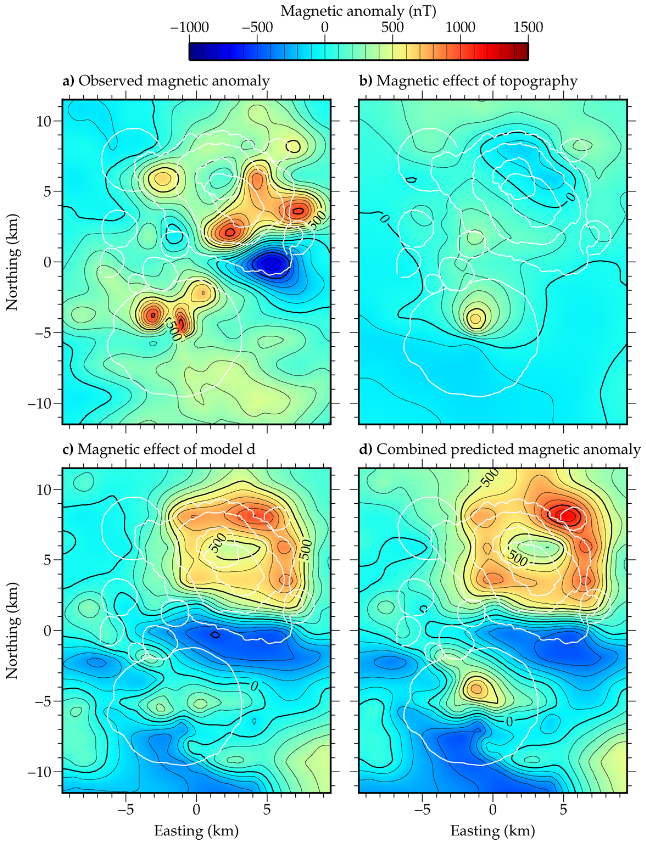

Figure 11. Results of magnetic anomaly modelling: (a) observed magnetic field anomaly; (b) magnetic effect of the topography assuming an upper crust with homogeneous magnetization of 3.2 Am^{-1}; (c) predicted magnetic anomaly calculated by assigning a constant magnetization of 3.6 Am^{-1} to prisms of model d with density ≥ 100 kg m^{-3}; (d) combined effect of (b) and (c). The white lines mark the locations of the Monowai cone, Monowai caldera and the major parasitic cones.

Ridge (Austin *et al.* 1989) suggest it comprises a thick compacted sequence of Oligocene–Miocene volcanoclastic sediments overlying an older Eocene arc. The subsurface high-density ring structure in the gravity models is interpreted as a ring dyke system, which links the high density body to the numerous cones dotting the rim and flanks of the Monowai caldera complex.

7.1 Relationship between tectonics and volcanism on the Kermadec Arc

The Monowai volcanic centre is located in a region of widespread extensional faulting related to ongoing back-arc spreading in the Havre Trough/Lau Basin. Wormald *et al.* (2012) use morphometric analysis to study a set of east-facing normal faults in the region west and north of Monowai, and show that the style of extension is transtensional. We have analysed the swath bathymetry data over a wider region around Monowai. With the aid of the morphometric parameters (Fig. 2) a conjugate set of west-facing normal faults was identified and mapped east of Monowai (Fig. 12). The faults range in length from a few hundred metres to 14 km and have an average strike 30° from the north, in agreement with the values measured by Wormald *et al.* (2012) on the east-facing faults to the west. The two sets of faults delimit a graben 10–20 km wide and at least 80 km long. The area northwest of Monowai is elevated and likely represents an uplifted horst block. Features such as these are widespread along the arc and backarc (Delteil *et al.* 2002) and form a series of en-echelon left-stepping horst and graben structures. The edge of another graben can be seen in the northwestern corner of Fig. 2(a). Delteil *et al.* (2002) argue that the oblique opening of the back-arc basin accommodates most or all of the oblique component of Indo-Australia/Pacific Plate convergence.

The characteristics of the normal faults vary greatly depending on the distance from the axis of the back-arc basin. The faults close to the axis are topped by volcanic ridges and cones. In contrast, along the active arc, the faults are non-volcanic and outcrop clearly on the seabed (Fig. 2). This change in faulting characteristics may indicate a fundamental change in the nature of melt migration in the crust. In the highly stretched and relatively thin crust of the backarc, magma exploits available extensional faults as direct pathways to the surface. In contrast, in the crust beneath the active arc, magma at shallow depth accumulates to form large magmatic intrusions, like the one found beneath Monowai, which feed the volcanic centres of the arc.

Monowai lies at the centre of one of these rift graben and is clearly affected by the tectonic regime in a number of ways. The Monowai caldera complex, including the two nested calderas MoC1 and MoC2, is elliptical with a long-axis striking roughly 130° (Wormald *et al.* 2012), perpendicular to the strike of the graben. This suggests that the caldera geometry is controlled to a first order by the direction of least horizontal compressive stress as is observed in analogue experiments of caldera collapse under compressive/extensive stress regimes (Holohan *et al.* 2005). The underlying pluton does not seem to be elongated in the same way as the caldera complex, again in agreement with predictions from analogue modelling.

A line joining Monowai cone and the resurgent dome inside the Monowai caldera complex strikes 20° from north and runs along the centre of the graben, suggesting that the locations of major eruptive vents may also be controlled by the tectonic fabric favouring alignment along-strike of the graben. On the other hand, the locations of other volcanic centres along the arc do not correlate with the locations of the graben. Instead they are found both inside graben and over horsts, suggesting that although the small-scale tectonic structure affects the shape of volcanic centres, it does not control their along-arc spacing.

7.2 Evolution of the Monowai volcanic centre

Two key outstanding questions regarding the plumbing system of Monowai volcanic centre are: (i) do the Monowai cone and caldera share a common shallow magmatic source? (ii) Are they or have they been active at the same time? In other words, what are their spatial and temporal relationship? Our potential field and morphological analysis sheds some light on these questions but also raises a number of new ones.

(i) The gravity inversion indicates that the Monowai caldera is underlain by a large magmatic intrusion and a ring dyke structure. The densities are compatible with a predominantly mafic composition. The intrusive body is thicker and wider beneath the southern half of the caldera and extends out to the southwest beneath a row of volcanic cones and towards Monowai cone.

(ii) Magnetic data analysis suggests that the Monowai cone, caldera and pluton were most likely formed within the Brunhes magnetic polarity (<0.78 Ma), although some parts of the volcanic complex may be older. Damping of magnetic anomalies in the northwest suggests this may be the oldest part of the volcanic centre.

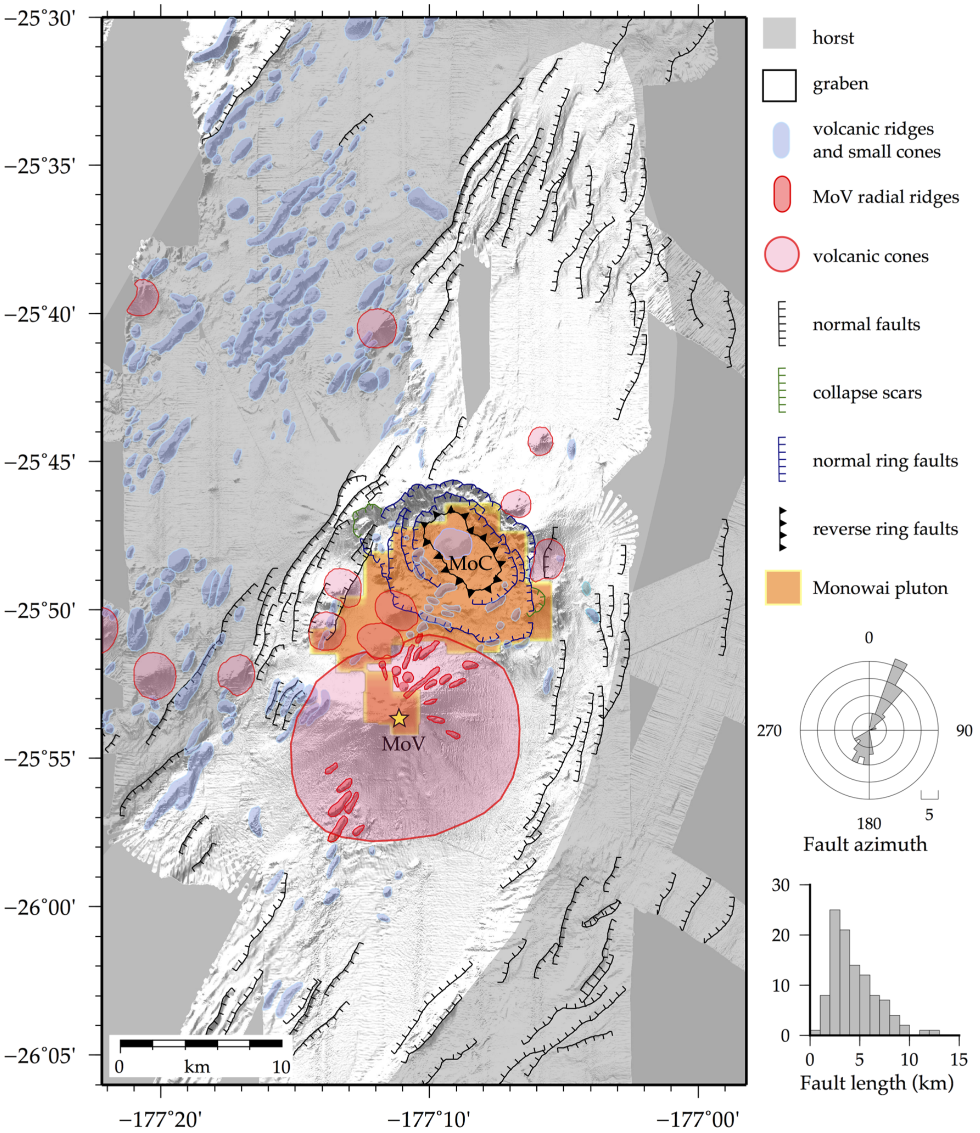

Figure 12. Structural interpretation map of the Monowai volcanic centre and surrounding region. Grey-shaded areas correspond to horst, white areas correspond to graben. The location of the 2011 Monowai cone summit is marked with a yellow star. Volcanic fissure ridges and small cones are marked in light blue. Larger cones are marked in pink. Radial fissure ridges on the flanks of Monowai cone are marked in red. The areal extent of the modelled Monowai pluton at 4 km depth (from Fig. 8d) is highlighted in orange.

(iii) The complex structure of the Monowai caldera suggests that it formed in multiple stages. The presence of numerous parasitic cones and volcanic ridges in different stages of preservation over the ring fault also suggests that activity on the ring dyke structure was prolonged.

(iv) The existence of fresh volcanic cones and active hydrothermal venting over the external ring fault in the southwest of the caldera suggests that there may be hot or partially molten rocks beneath this area (Leybourne *et al.* 2012). This observation is supported by evidence of relative demagnetization.

(v) The volume of Monowai cone closely matches the volume of the void created by the collapse of the Monowai caldera. The alignment of the Monowai cone and caldera along the tectonic fabric and perpendicular to the direction of rifting may facilitate the propagation of dykes and the lateral migration of magma between them. The presence of volcanic ridges on the northern flank of Monowai Volcano also indicates the presence of a system of fissures connecting the two volcanic edifices.

(vi) Gravity inversion is unable to provide any constraints on the presence of partial melt since gravity anomalies are only weakly sensitive to melt fraction. On the other hand, the results of the magnetic data analysis require the pluton to be below the Curie temperature (≃575 °C for gabbro, Kent *et al.* 1978). We can, therefore, infer that it is most likely to comprise solid gabbroic cumulate, although regions of partial melt may exist within it.

The simplest interpretation of these observations is that the Monowai pluton represents a long-lived shallow magma chamber system which fed the Monowai caldera complex and which is, today, mostly solidified. The pluton may have formed incrementally, by intrusion of successive batches of magma. The observed protrusion on southwestern end of the density anomaly (Fig. 9) may correspond to a recent batch of magma laterally feeding the current eruption at Monowai cone and some of the youngest parasitic cones, as well as driving hydrothermal activity on the southwest rim of the caldera. Alternatively, Monowai cone may be fed by a distinct small or deeper magma chamber perhaps corresponding to the small positive density anomaly observed beneath Monowai cone in some of our models (Fig. 9b). Supporting evidence for the presence of a shallow magma chamber beneath Monowai cone comes from the observation of radial volcanic fissure ridges on its slopes, which may indicate a recent and perhaps ongoing period of inflation, causing radial cracks to develop (Walter & Troll 2001).

The high eruptive rates documented by Watts *et al.* (2012) suggest that if a shallow magma chamber is present beneath Monowai cone it may lead to formation of a summit caldera similar to those observed at Volcano 14 and Volcano 19 in the southern Tonga arc (Massoth *et al.* 2007). Additional evidence may come from thermobarometry constraints on the storage conditions of Monowai magma prior to eruption and from monitoring of microseismicity.

The complex shape of Monowai caldera has been previously interpreted as a nested caldera system, with a younger smaller caldera (MoC2) nested inside an older larger caldera (MoC1). However, analysis of the caldera morphology and comparison with analogue models of caldera collapse and resurgence (Walter & Troll 2001; Geyer *et al.* 2006; Acocella 2007) suggest that its structure can be explained by prolonged collapse of a single, long-lived caldera perhaps complicated by repeated episodes of inflation and deflation and by mass wasting along the steep caldera walls. Initially, the emplacement of this large intrusion at 3–6 km depth would have caused up-doming of the seabed and the formation of concentric thrust faults and radial cracks, as observed in analogue models of volcanic inflation and collapse (Walter & Troll 2001). Partial evacuation via isolated conduits and perhaps the early ring fault caused underpressure in the magma chamber and initial subsidence of the caldera roof along an outward-dipping reverse ring fault (Fig. 12), corresponding to the sides of the inner caldera. Further subsidence of the caldera roof caused the formation of an outer inward-dipping normal ring fault. Roche *et al.* (2000) predict the development of a system of concentric ring faults for small roof aspect ratios similar to that determined from our density model (aspect ratio = 0.2–0.3).

Repeated collapse events, perhaps separated by replenishment of the magma chamber and inflation, may have caused the caldera rim to migrate outwards. This would have created a system of inward-dipping normal ring faults and a circular zone between the outer and inner ring fault consisting of small crescent-shaped half-graben forming the outer depression (Fig. 13). The numerous flat-lying areas around the outer depression, which have previously been interpreted as remnants of the outer caldera floor, may instead be sediment pockets filling the small basins resulting from subsidence-related extension.

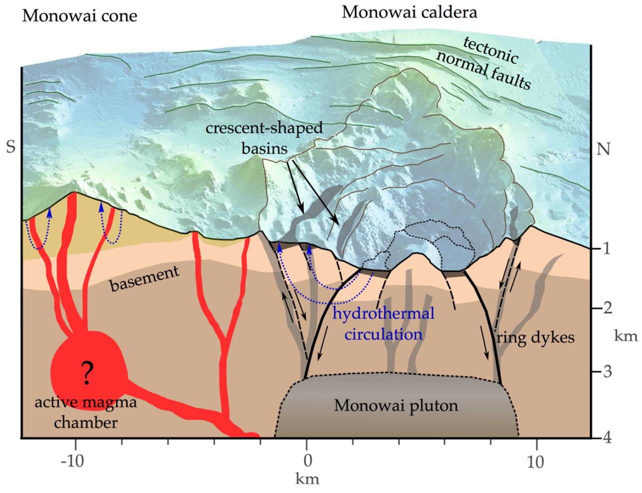

Figure 13. Schematic structural interpretation of the shallow plumbing system of the Monowai volcanic centre.

Geyer *et al.* (2006) show that for small caldera roof aspect ratios, only a relatively small percentage (10–30 per cent) of the magma chamber volume needs to be erupted to trigger caldera collapse. The volume of eruptive products of Monowai caldera is difficult to quantify, but it is likely to be of the order of the volume of the caldera depression (32 km^3). Assuming a magma chamber volume of 200–300 km^3, equal to our preferred volume range estimate for the main unit of the Monowai pluton, leads to an erupted magma fraction of 10–16 per cent, which is at the low end of the above range. Other factors (e.g. regional stress) might have contributed to early caldera collapse. In such a scenario much of the magma would have remained unerupted in the subsurface and solidified to form the Monowai pluton. Thermal contraction of such a large solidifying magma body and deformation caused by its gravitational load, might have contributed to subsidence of the caldera roof.

Dredge samples collected during cruise NZAPLUME III in 2004 September–October indicate that the central dome is composed of tholeitic basalt (Graham *et al.* 2008). This observation led to the conclusion that the dome represents the product of one or more post-collapse eruptions following replenishment of the magma chamber with mafic magma. However, the mound morphology does not resemble that of a volcanic cone, its plan form is polygonal and its sides are approximately planar instead of being concave upward. The slope break at its base is extremely sharp which suggests that it may be of tectonic origin. The caldera floor around the mound is divided into at least three separate polygonal patches offset vertically by a few tens of metres. A similar morphology is observed in analogue models of caldera formation if collapse is preceded by doming or resurgence. In this case radial fractures may propagate outward and break the caldera roof into polygonal blocks, which may become offset during roof collapse. The central dome may correspond to an uplifted and tilted caldera roof block. Alternatively it may represent a remnant volcanic plug of the proto-Monowai Volcano. In its early stage, the eruptive products may have been basaltic, similar to those of present-day Monowai cone. Then, as the system matured, differentiation of magma may have led to the generation and eruption of more evolved lavas like those sampled along the caldera rim (Timm *et al.* 2011). It is unclear whether a significant proto-Monowai cone existed at the location of the current caldera, which would have been destroyed by the caldera collapse.

8 CONCLUSIONS

Swath bathymetry surveys of Monowai show that it comprises one of the world's most active submarine volcanic cones and one of the largest known submarine calderas. The caldera is associated with a Bouguer gravity anomaly high of up to 30 mGal and wavelength of 20 km, and magnetic anomaly highs and lows of +1400 and −800 nT. The gravity high is attributed to a shallow dense body (2650–2850 kg m^{-3}) of probably gabbroic or other mafic rock, and represents a solidified or partly solidified magma chamber system (the Monowai pluton) and a ring dyke structure. The total volume of the dense body is 200–300 km^3, and analysis of the magnetic anomalies suggests a maximum age of 0.78 Myr.

We interpret the Monowai caldera complex to have resulted from the prolonged collapse of a single caldera structure after partial evacuation of the underlying magma chamber, perhaps over multiple stages intercalated by periods of resurgence. The central mound, previously interpreted as a resurgent dome, may instead be the result of breaking and tilting of the caldera floor during collapse or may represent a remnant volcanic plug.

The Monowai volcanic centre lies inside a graben, part of a large system of en-echelon left-stepping horst-graben structures running along the length of the Tonga-Kermadec arc and the back-arc of the Havre Trough and Lau Basin. The regional extensional stress regime influences the shape of the caldera complex, which is elliptical with its long axis parallel to the direction of least horizontal compressive stress. The underlying intrusion does not appear to be similarly elongated.

It is unclear whether the current eruption at Monowai cone is fed laterally from a recent batch of magma adjacent to the Monowai pluton, or whether its source is a smaller magma chamber located beneath the eruptive vent. The latter hypothesis is supported by observations of radial fissure ridges on its flanks, which we interpret as radial cracks caused by inflation of an underlying magma body.

The discovery of the Monowai pluton and the overlying ring dyke structure fills a large gap in our understanding of the plumbing system of Monowai and leads to a multi-phase model for its evolution, from initial crustal inflation to present day:

Phase 1: Crustal inflation, with initial mafic magmatism that gradually becomes more silicic as the magma differentiates and a layered cumulate pluton develops.

Phase 2: Caldera formation and collapse of the caldera roof into the magma chamber along a fault system, comprising an inner outward-dipping reverse ring fault and an outer inward-dipping normal ring fault.

Phase 3: Additional cycles of inflation and caldera subsidence accompanied by caldera floor filling and lateral wall collapse, lead to the development of a complex system of crescent-shaped half-graben and tilted blocks between the two major ring faults.

Phase 4: A new pulse of mafic magma and migration of eruptive source to the south forms the present-day Monowai cone.

ACKNOWLEDGEMENTS

We are grateful to the Captain Lutz Mallon and the officers, crew and shipboard scientific party of the R/V Sonne for their help at sea and to Antonio Camacho for providing his gravity inversion code Growth 2.0. The figures were constructed using GMT (Wessel & Smith 1991) and Fledermaus. The project was funded by UK Natural Environment Research Council grants NE/F005318/1 and NE/F004273/1. The bathymetry and potential field data are freely available for download from the NERC's British Oceanographic Data Centre (http://www.bodc.ac.uk).

REFERENCES

Acocella, V., 2007. Understanding caldera structure and development: an overview of analogue models compared to natural calderas, *Earth-Sci. Rev.,* **85**(3), 125–160.

Austin, J.A., Taylor, F.W. & Cagle, C.D., 1989. Seismic stratigraphy of the central Tonga Ridge, *Mar. Petrol. Geol.,* **6**(1), 71–92.

Bhattacharyya, B.K., 1964. Magnetic anomalies due to prism-shaped bodies with arbitrary polarization, *Geophysics,* **29**(4), 517–531.

Bott, M. & Tuson, J., 1973. Deep structure beneath the Tertiary volcanic regions of Skye, Mull and Ardnamurchan, north-west Scotland, *Nat. Phys. Sci.,* **242,** 114–116.

Budetta, G., Nunziata, C. & Rapolla, A., 1983. A gravity study of the island of Vulcano, Tyrrhenian Sea, Italy, *Bull. Volcanol.,* **46**(2), 183–192.

Camacho, A.G., Montesinos, F.G. & Vieira, R., 2000. Gravity inversion by means of growing bodies, *Geophysics,* **65**(1), 95–101.

Camacho, A., Montesinos, F. & Vieira, R., 2002. A 3-D gravity inversion tool based on exploration of model possibilities, *Comput. Geosci.,* **28**(2), 191–204.

Camacho, A.G., Fernandez, J. & Gottsmann, J., 2011. The 3-D gravity inversion package GROWTH2.0 and its application to Tenerife Island, Spain, *Comput. Geosci.,* **37**(4), 621–633.

Caress, D.W. & Chayes, D.N., 1995. New software for processing sidescan data from sidescan-capable multibeam sonars, in *Proceedings of the OCEANS'95. MTS/IEEE. Challenges of Our Changing Global Environment Conference,* Vol. **2,** pp. 997–1000, IEEE.

Carlson, R.L. & Raskin, G.S., 1984. Density of the ocean crust, *Nature,* **311**(5986), 555–558.

Carmichael, R.S., 1982. *Magnetic Properties of Mineral and Rocks, Vol. 2, Chap. 2,* pp. 229–287, CRC Press.

Chadwick, W.W. Jr., Wright, I.C., Schwarz-Schampera, U., Hyvernaud, O., Reymond, D. & de Ronde, C.E.J., 2008. Cyclic eruptions and sector collapses at Monowai submarine volcano, Kermadec arc: 1998–2007, *Geochem. Geophys. Geosyst.,* **9**(10), doi:10.1029/2008GC002113.

Christensen, N.I. & Mooney, W.D., 1995. Seismic velocity structure and composition of the continental crust: a global view, *J. geophys. Res.-Solid Earth,* **100**(B6), 9761–9788.

Connor, C.B. & Williams, S.N., 1990. Interpretation of gravity anomalies, Masaya caldera complex, Nicaragua, in *Proceedings of the Transactions of the 12th Caribbean Conference,* St Croix, Virgin Islands, pp. 495–502.

Contreras-Reyes, E., Grevemeyer, I., Watts, A.B., Flueh, E.R., Peirce, C., Moeller, S. & Papenberg, C., 2011. Deep seismic structure of the Tonga subduction zone: implications for mantle hydration, tectonic erosion, and arc magmatism, *J. geophys. Res.-Solid Earth,* **116**(B10), doi:10.1029/2011JB008434.

Davey, F.J., 1980. The Monowai seamount—an active submarine volcanic centre on the Tonga-Kermadec Ridge, *New Zeal. J. Geol. Geophys.,* **23**(4), 533–536.

Delteil, J., Ruellan, E., Wright, I. & Matsumoto, T., 2002. Structure and structural development of the Havre Trough (SW Pacific), *J. geophys. Res.,* **107**(B7), 2143–2160.

Deplus, C., Bonvalot, S., Dahrin, D., Diament, M., Harjono, H. & Dubois, J., 1995. Inner structure of the Krakatau volcanic complex (Indonesia) from gravity and bathymetry data, *J. Volc. Geotherm. Res.,* **64**(1), 23–52.

Eaton, G.P., Christiansen, R.L., Iyer, H., Pitt, A.D., Mabey, D.R., Blank Jr, H.R., Zietz, I. & Gettings, M.E., 1975. Magma beneath Yellowstone National Park, *Science,* **188**(4190), 787–796.

Embley, R.W. *et al.*, 2005. Hydrothermal systems on Kermadec arc volcanoes revealed by PISCES V submersible dives, *AGU, Fall Meeting, Abstracts,* **44**(A04E).

Emeleus, C.H., Cheadle, M.J., Hunter, R.H., Upton, B.G.J. & Wadsworth, W.J., 1996. The Rum layered suite, *Dev. Petrol.,* **15,** 403–439.

Finn, C. & Williams, D.L., 1982. Gravity evidence for a shallow intrusion under Medicine Lake volcano, California, *Geology,* **10**(10), 503–507.

Flueh, E.R. & Kopp, H., 2007. *SO192/2—Mango,* Tech. rep., Ber.-Rep., Inst. fur Geowiss., Universitat Kiel.

Fumerato, A., Norris, R., Kam, M. & Fernander, C., 1976. *Gravity profile and the intrusive zone, in Hawaii Geothermal Project Initial Phase II,* Tech. rep., Univ. Hawaii.

Gettings, M.E. & Griscom, A., 1988. Gravity model studies of Newberry volcano, Oregon, *J. geophys. Res.,* **93**(B9), 10 109–10 118.

Geyer, A., Folch, A. & Martí, J., 2006. Relationship between caldera collapse and magma chamber withdrawal: an experimental approach, *J. Volc. Geotherm. Res.,* **157**(4), 375–386.

Graham, I.J., Reyes, A.G., Wright, I.C., Peckett, K.M., Smith, I.E.M. & Arculus, R.J., 2008. Structure and petrology of newly discovered volcanic centers in the northern Kermadec-southern Tofua arc, South Pacific Ocean, *J. geophys. Res.,* **113**(B8), B08S02, doi:10.1029/2007jb005453.

Haase, K.M., Worthington, T.J., Stoffers, P., Garbe-Schonberg, D. & Wright, I., 2002. Mantle dynamics, element recycling, and magma genesis beneath the Kermadec Arc-Havre Trough, *Geochem. Geophys. Geosyst.,* **3**(11), doi:10.1029/2002GC000335.

Hallinan, S.E., 1991. Gravity studies of the Guayabo Caldera and the Miravalles geothermal field, Costa Rica., *PhD thesis,* Open University.

Hallinan, S.E., 1993. Nonchaotic collapse at funnel calderas: gravity study of the ring fractures at Guayabo caldera, Costa Rica, *Geology,* **21**(4), 367–370.

Hayes, G.P., Wald, D.J. & Johnson, R.L., 2012. Slab1.0: a three-dimensional model of global subduction zone geometries, *J. geophys. Res.,* **117,** B01302, doi:10.1029/2011JB008524.

Holohan, E.P., Troll, V.R., Walter, T.R., Münn, S., McDonnell, S. & Shipton, Z.K., 2005. Elliptical calderas in active tectonic settings: an experimental approach, *J. Volc. Geotherm. Res.,* **144**(1), 119–136.

Kane, M.F., Mabey, D.R. & Brace, R.-L., 1976. A gravity and magnetic investigation of the Long Valley caldera, Mono County, California, *J. geophys. Res.,* **81**(5), 754–762.

Kent, D.V., Honnorez, B., Opdyke, N.D. & Fox, P.J., 1978. Magnetic properties of dredged oceanic gabbros and the source of marine magnetic anomalies, *Geophys. J. R. astr. Soc.,* **55**(3), 513–537.

LaFehr, T.R., 1965. Gravity, isostasy, and crustal structure in the southern Cascade Range, *J. geophys. Res.,* **70**(22), 5581–5597.

Lagios, E., Sakkas, V., Novali, F., Bellotti, F., Ferretti, A., Vlachou, A. & Dietrich, V., 2013. SqueeSAR and GPS ground deformation monitoring of Santorini Volcano (1992–2012): tectonic implications, *Tectonophysics,* **594,** 38–59.

Leybourne, M.I. *et al.*, 2012. Submarine magmatic-hydrothermal systems at the Monowai volcanic center, Kermadec arc, *Econ. Geol.,* **107**(8), 1669–1694.

Massoth, G. *et al.*, 2007. Multiple hydrothermal sources along the south Tonga arc and Valu Fa Ridge, *Geochem., Geophys., Geosyst.,* **8**(11), doi:10.1029/2007GC001675.

Micallef, A., Berndt, C., Masson, D.G. & Stow, D.A.V., 2007. A technique for the morphological characterization of submarine landscapes as exemplified by debris flows of the Storegga Slide, *J. geophys. Res.: Earth Surf. (2003–2012),* **112**(F2), F02001, doi:10.1029/2006JF000505.

Neteler, M., Bowman, M.H., Landa, M. & Metz, M., 2011. GRASS GIS: a multi-purpose Open Source GIS, *Environmental Modelling & Software,* **31,** 124–130.

Nishimura, S., Abe, E., Nishida, J., Yokoyama, T., Dharma, A., Hehanussa, P. & Hehuwat, F., 1984. A gravity and volcanostratigraphic interpretation of the Lake Toba region, North Sumatra, Indonesia, *Tectonophysics,* **109**(3), 253–272.

Parker, R.L., 1973. The rapid calculation of potential anomalies, *Geophys. J. R. astr. Soc.,* **31**(4), 447–455.

Pick, M., Picha, J. & Vyskolic, V., 1973. *Theory of the Earth's Gravity Field,* Elsevier.

Roche, O. & Druitt, T.H., 2001. Onset of caldera collapse during ignimbrite eruptions, *Earth planet. Sci. Lett.,* **191**(3), 191–202.

Roche, O., Druitt, T.H. & Merle, O., 2000. Experimental study of caldera formation, *J. geophys. Res.-Solid Earth (1978–2012),* **105**(B1), 395–416.

Rona, P.A., 1978. Criteria for recognition of hydrothermal mineral deposits in oceanic crust, *Econ. Geol.,* **73**(2), 135–160.

de Ronde, C.E.J. *et al.*, 2005. Evolution of a submarine magmatic-hydrothermal system: brothers volcano, southern Kermadec arc, New Zealand, *Econ. Geol.,* **100**(6), 1097–1133.

Ryan, M.P., Koyanagi, R.Y. & Fiske, R.S., 1981. Modeling the three-dimensional structure of macroscopic magma transport systems: application to Kilauea Volcano, Hawaii, *J. geophys. Res.-Solid Earth (1978–2012),* **86**(B8), 7111–7129.

Rymer, H., 1985. Gravity studies of sub-surface structures and evolution of active volcanoes in Costa Rica., *PhD thesis,* Open University.

Rymer, H. & Brown, G.C., 1986. Gravity fields and the interpretation of volcanic structures: geological discrimination and temporal evolution, *J. Volc. Geotherm. Res.,* **27**(3), 229–254.

Sandwell, D.T. & Smith, W.H.F., 2009. Global marine gravity from retracked Geosat and ERS-1 altimetry: ridge segmentation versus spreading rate, *J. geophys. Res.,* **114,** doi:10.1029/2008JB006008.

Stoffers, P. & Wright, I. Shipboard Scientific Party, 1999. Cruise Report SONNE 135: Havre Trough Taupo Volcanic Zone: Tectonic, magmatic and hydrothermal processes, Tech. rep., Ber.-Rep., Inst. fur Geowiss., Universitat Kiel.

Timm, C., Graham, I.J., de Ronde, C. E.J., Leybourne, M.I. & Woodhead, J., 2011. Geochemical evolution of Monowai volcanic center: new insights into the northern Kermadec arc subduction system, SW Pacific, *Geochem. Geophys. Geosyst.,* **12**(8), doi:10.1029/2011GC003654.

Tivey, M.A. & Dyment, J., 2010. The magnetic signature of hydrothermal systems in slow spreading environments, diversity of hydrothermal systems on slow spreading ridges, *Geophys. Monogr. Ser.,* **188,** 43–66.

Tontini, F.C., Davy, B., De Ronde, C.E.J., Embley, R.W., Leybourne, M. & Tivey, M.A., 2012. Crustal magnetization of Brothers volcano, New Zealand, measured by autonomous underwater vehicles: geophysical expression of a submarine hydrothermal system, *Econ. Geol.,* **107**(8), 1571–1581.

Troll, V.R., Emeleus, C.H. & Donaldson, C.H., 2000. Caldera formation in the Rum central igneous complex, Scotland, *Bull. Volcanol.,* **62**(4–5), 301–317.

Walter, T.R. & Troll, V.R., 2001. Formation of caldera periphery faults: an experimental study, *Bull. Volcanol.,* **63**(2–3), 191–203.

Watts, A.B. *et al.*, 2012. Rapid rates of growth and collapse of Monowai submarine volcano in the Kermadec Arc, *Nat. Geosci.,* **5**(7), 510–515.

Wessel, P. & Smith, W.H.F., 1991. Free software helps map and display data, *EOS, Trans. Am. geophys. Un.,* **72**(41), 441–446.

Wilson, M.F.J., O'Connell, B., Brown, C., Guinan, J.C. & Grehan, A.J., 2007. Multiscale terrain analysis of multibeam bathymetry data for habitat mapping on the continental slope, *Mar. Geod.,* **30**(1–2), 3–35.

Wormald, S.C., Wright, I.C., Bull, J.M., Lamarche, G. & Sanderson, D.J., 2012. Morphometric analysis of the submarine arc volcano Monowai (Tofua-Kermadec Arc) to decipher tectono-magmatic interactions, *J. Volc. Geotherm. Res.,* **239,** 69–82.

Wright, I.C. & Gamble, J.A., 1999. Southern Kermadec submarine caldera arc volcanoes (SW Pacific): caldera formation by effusive and pyroclastic eruption, *Mar. Geol.,* **161**(2–4), 207–227.

Wright, I.C. *et al.*, 2008. Collapse and reconstruction of Monowai submarine volcano, Kermadec arc, 1998–2004, *J. geophys. Res.,* **113**(B8), doi:10.1029/2007JB005138.

Yokoyama, I., 1958. Gravity survey on Kuttyaro caldera lake, *J. Phys. Earth,* **6,** 75–79.

Yokoyama, I., 1961. Gravity survey on the Aira caldera, Kyushu - Japan, *Nature,* **191,** 966–967.

Yokoyama, I., 1963. Structure of caldera and gravity anomaly, *Bull. Volcanol.,* **26**(1), 67–72.

Yokoyama, I., 1969. The subsurface structure of Oosima volcano, Izu, *J. Phys. Earth,* **17**(1), 55–68.

Yokoyama, I. & Tajima, H., 1957. A gravity survey on Volcano Mihara, Oosima Island by means of a Worden gravimeter, *Bull. Earthq. Res. Inst.,* **35,** 23–33.